Mechanical Systems and Signal Processing 224 (2025) 111980

Contents lists available at ScienceDirect

Mechanical Systems and Signal Processing

journal homepage: www.elsevier.com/locate/ymssp

Numerical and experimental investigations on the dynamic behavior of a rotor-AMBs system considering shrink-fit assembly

Yang Zhou [a], Yuanping Xu [a,*], Jin Zhou [a], Yue Zhang [a], Jarir Mahfoud [b,*]

[a] College of Mechanical and Electrical Engineering, Nanjing University of Aeronautics and Astronautics, Nanjing 210016, China
[b] INSA-Lyon, CNRS UMR5259, LaMCoS, F-69621 Villeurbanne Cedex, France

ARTICLE INFO

Communicated by Paolo Pennacchi

Keywords:
Shrink fit
Contact model
Interface contact
Active magnetic bearings
Vibration analysis

ABSTRACT

Rotor-Active Magnetic Bearings (rotor-AMBs) systems nowadays have been widely used in turbomachinery where different methods for assembly were used such as impeller mounted using shrink-fit. In our experiments we noticed that the conditions of shrink-ft assembly can introduce instabilities on the levitated rotor at rest. To understand and give recommendations (on the assembly conditions), a numerical model was developed and then was validated experimentally. The effect of the shrink-fit interface contact was modelled as a contact force acting on the rotor-AMBs system introduced by distributed spring units with a given contact stiffness. Considering that there was partial separation in the contact interface due to the AMBs levitating forces, a novel contact force model related to contact status was established by calculating the real-time contact area. A microscopic contact model based on fractal theory was developed to calculate the contact stiffness. The model developed was then validated experimentally simulating the levitating rotor at rest. The rotor response was analyzed in frequency domains by applying the different conditions of shrink-fit interference and contact length. The shrink-fit contact conditions influenced the system stability and made the fourth bending mode unstable. The increase of shrink-fit interference and contact length decreased closed-loop system stability and increased the amplitude of the rotor vibration response. The model reliability was assessed and a stable region using combinations of shrink-fit parameters on the assembly conditions based on the results of stability analysis was established.

Nomenclature

a_{rc}, a_{rl}	critical real contact area, the maximum real contact area of the contact surface/m^2
a_u, a_{uc}, a_{ul}	truncated area, the critical truncated contact area, the maximum truncated area of the microcontact/m^2
A_{33}, B_{33}, C_{33}	unknown coefficients of the equation describing plane PA
A_{44}, B_{44}, C_{44}	unknown coefficients of the equation describing plane PB
A_a	nominal area of the contact surface/m^2
A_m	area of one pole of the radial active magnetic bearing/m^2
A_{rc}	real contact area of the contact surface/m^2
A_{sr}	state matrix of the state space model of the rotor-AMBs system considering interface contact and control
C_0	radial air gap between the rotor and the AMB/m
D	fractal dimension

(continued on next page)

* Corresponding authors.
E-mail addresses: ypxu@nuaa.edu.cn (Y. Xu), jarir.mahfoud@insa-lyon.fr (J. Mahfoud).

https://doi.org/10.1016/j.ymssp.2024.111980
Received 18 February 2024; Received in revised form 6 August 2024; Accepted 21 September 2024
Available online 29 September 2024

Nomenclature (*continued*)

D_{di}, D_{do}	inner diameter and outer diameter of the disk/mm
D_{ri}, D_{ro}	inner diameter and outer diameter of the rotor/mm
$\overline{\mathrm{E}}$	equivalent elastic modulus of the contact surface/Pa
E_d, E_r	elastic modulus of the disk and the rotor/Pa
f_{amb}	attractive magnetic force along the action line/N
f_n, f_t	normal and tangential contact loads acting on a single microcontact/N
f_z	cut-off frequency of the power amplifier/Hz
F_n	normal load applied on the contact surface/Pa
F_{sc}	vector of the forces generated by the interface contact
F_{AMB}	vector of the forces generated by AMBs
G	fractal roughness/m
$\overline{\mathrm{G}}$	equivalent shear modulus of the contact surface/Pa
G_d, G_r	shear modulus of the disk and the rotor/Pa
H_s	transfer function of the feedback control
i	frequency index of the surface profile function
i_a	control current of AMB/A
k_a	gain of the power amplifier/A•V^{-1}
k_h	displacement stiffness of AMB/N•m^{-1}
k_i	current stiffness of AMB/N•A^{-1}
k_n, k_t	normal and the tangential contact stiffness of a single micro-contact interacting with a rigid plane/N•m^{-3}
k_s	gain of the displacement sensor/V•m^{-1}
k_{sf}, k_{sq}	normal and the tangential contact stiffness of the massless spring unit/N•m^{-3}
Ks	gain matrix of the forces generated by the interface contact
K_n, K_t	total normal and tangential contact stiffness/N•m^{-1}
K_P, K_I, K_D	proportional, the integral and the derivative gains of the PID controller
K_{Es}	equivalent contact stiffness matrix
Ks_x, Ks_y, Ks_α, Ks_β	gains of the forces generated by the interface contact in x ,y, α, β directions
l_{s1}, l_{s2}	lines formed by the intersection between outer surface, end faces of rotor, and inner surface of disk
L	sample length of the surface profile
L_d	thickness of the disk/mm
L_s, L_{sr}	contact length of shrink-fit assembly and its half/m
M_R, K_R, C_R	mass, stiffness and damping matrices of the rotor
n	size distribution function of microcontacts
N_c	turns per coil of a pair of poles in AMB
p_e, p_p	normal contact load of a single microcontact with elastic and plastic deformation/Pa
P	Power Spectral Density of the surface profile/μm^3
P_c	pressure of the shrink-fit assembly/Pa
q_r, q_p, q_q, q_s	displacement vectors of rotor, node p, node q and sensor nodes
r_u	truncated radius of the undeformed asperity/m
R_c	radius of the curvature of the microcontact/m
R_s	nominal radius of the shrink-fit contact/m
R_{do}, R_{ri}	outer diameter of the disk, inner diameter of the rotor/mm
T_s, T_a, T_e, T_{sc}	transfer matrixes of the sensor nodes, AMB nodes, interface contact nodes, node p
T_D	derivative time constant of the PID controller
U_s, Δu	energy generated by the deformation of all spring units and single spring unit/J
$W_1(\theta_3)$, $W_2(\theta_3)$	function of line l_{s2}
x_{C}, y_{C}, z_{C}	coordinates of Node C in x ,y, z directions in the absolute coordinate system
x_{D}, y_{D}, z_{D}	coordinates of Node D in x ,y, z directions in the absolute coordinate system
x'	coordinate along the surface
z_1	height of the rough surface/m
$z_3(\theta_3)$	function of line l_{s1}
λ	closed-loop system eigenvalues
μ	friction coefficient of the contact surface
μ_0	permeability of vacuum/H•m^{-1}
ψ	domain extension factor
ω_p	wavevector of surface profile/μm^{-1}
υ_d, υ_r	Poisson ratios of the disk and the rotor
τ	elastic deformation in the tangential direction for a single micro-contact interacting with a rigid plane/m
δ, δ_{uc}	deformation of an individual asperity, critical deformation of an individual asperity/m
δ_c	shrink-fit interference/m
$\phi_{1,i}$	randomly phase corresponds to the different cutoff frequency of the profile/rad•s^{-1}
σ_s	yield strength of the disk material/Pa
Δx, Δy, Δz	deformation of the spring unit in x ,y, z directions in the absolute coordinate system/m
Δx_{qp}, Δy_{qp}, $\Delta \alpha_{qp}$, $\Delta \beta_{qp}$	relative displacement between Node p and Node q in x ,y, α, β directions/m
θ_3, θ_{31}, θ_{32}	coordinate along the circumferential direction, critical degree of the real contact region/°

1. Introduction

Active magnetic bearings (AMBs) have been widely used in centrifugal gas compressors and other turbomachinery applications [1]. In these rotating machineries, several methods could be used to assemble the different components and particularly shrink-fit

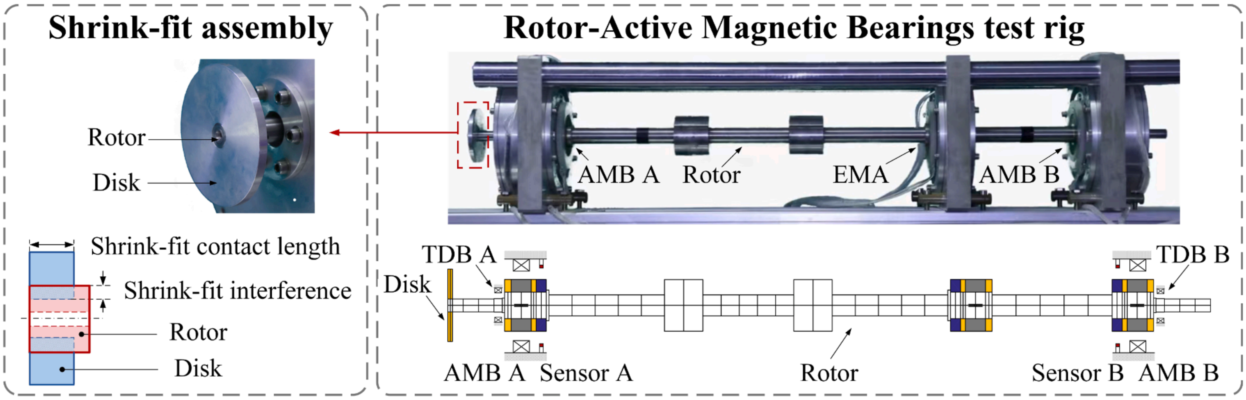

Fig. 1. Rotor-AMBs test rig.

assembly. The shrink-fit could generally be characterized by its interference and contact length as shown in Fig. 1 [2]. We noticed that, when the shrink-fit interference is relatively small (there is contact pressure), a possible relative displacement is induced by the AMB levitating forces, that could lead to the excitation of the structure and could introduce instability for modes that are on the limit of stability. Usually, when the shrink-fit is tight enough, there is contact pressure but no relative displacement. On the other hand, when the shrink fit was changed to clearance fit, there is relative displacement but no contact pressure. But in these two cases, the rotor remains stable when levitated. Yannick Paul et al. mentioned that the poor connection between rotor and the impeller may cause high-frequency vibration during levitation in the expander-compressors with AMBs[3]. Therefore, the cause of this vibration is the coupling between the shrink-fit interface contact and the AMB levitating forces [34]. The motivation of this paper is to investigate the influences of shrink-fit parameters on the stability of the rotor-AMBs system and to determine the suitable shrink-fit parameters to keep the system stable.

In shrink-fit modelling, there are three main approaches:

(1) The first introduced an equivalent material layer as an intermediate medium to reflect the contact effect [5]. The mechanical property of the contact interface of shrink-fit assembly was characterized by adjusting the parameters (elastic modulus, Poisson's ratio, density) of the equivalent material layer;
(2) Model updating method, where the shaft with shrink-fit lamination was modelled with an equivalent material, the Young's modulus and density of the new material were updated based on modal testing results [6] and equations [7], respectively. This method ensured the accuracy of rotor's frequency response but ignored the contact effect;
(3) Spring element method, where the stiffness coefficient of the spring (called contact stiffness) had to be adjusted experimentally. This is the approach we used in this study.

The spring element method can be divided into two approaches: a concentrated spring element and a distrusted spring element [8].

(a) In the concentrated model, all nodes of the surface are in contact and the contact pressure and deformation are uniformly distributed. Jafri [9] and Francesco Sorge [1011] studied the sub-synchronous rotor dynamic instability caused by the shrink-fit interface. The effect of shrink-fit contact was modelled as an angular spring and angular damper that induced slippage friction forces act as destabilizing cross-coupled moments. Reception Coupling Substructure Analysis (RCSA) method is widely applied in tool-holder structure modelling. In this method, the shrink-fit contact was modelled as a spring element to connect the tool substructure and holder substructure [1213]. The contact stiffness heavily relied on the experimental identification of the parameters. Wei [4] considered the influence of shrinkage fit between shaft and rigid disk as angular spring and angular damper, which generate rotational disturbance on the shaft.
(b) In the distributed spring model, the contact state of all nodes in the contact surface are anisotropic (some nodes are in contact and others non). For higher accuracy, Sikanen [1415] built a model by applying three-dimensional element, which can better simulate the contact property of shrink-fit rotor. The microslip model is widely applied in spigot structure. In the study [1617], the model considered the stick–slip statuses of spigot by introducing a Jenkins element, therefore was able to describe the spigot joint's damping nonlinearity. Thereby, spring element methods are found to be more adapted since the spring element can describe the relative displacement and the contact pressure efficiently.

Two approaches are usually used to determine the contact stiffness, either updating the contact stiffness based on modal testing results [1819] where the identification of the contact stiffness based on modal properties is accurate, but it is not convenient to identify the contact stiffness under different shrink-fit interferences; or establishing a microscopic contact model, where the relationship between the contact stiffness and shrink-fit interference is obtained based on fractal theory and hertz contact model. The fractal theory [20] was used to describe the contact surface profile. The stiffness of the spring in RCSA model [21] and finite element model [2223]

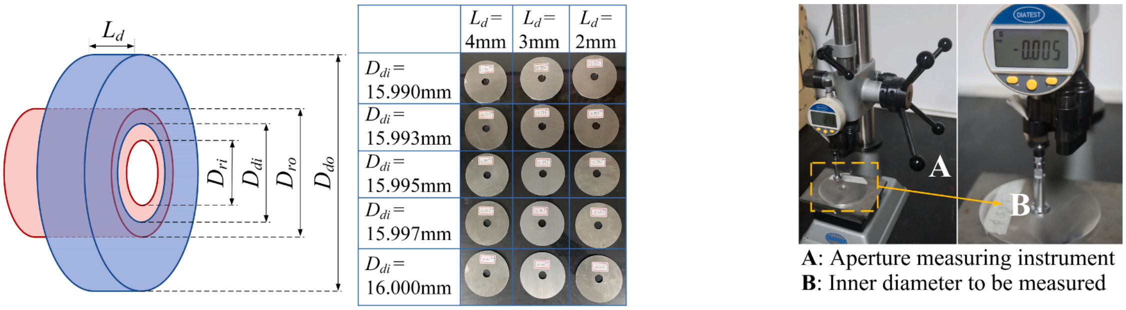

(a) Disks manufactured (b) Measurement of inner diameter

Fig. 2. The diagram of shrink-fit disks.

were calculated based on fractal contact theory that will be presented later. In these studies, the influence of shrink-fit interference, rotational speed, material properties and contact length on contact stiffness were investigated. The contact stiffness can be calculated under different contact pressure, but an accurate description of surface profile is necessary.

AMB system was not considered in the researches mentioned previously. Therefore, a modelling of the rotor-AMBs system (mechatronic model) with shrink fit assembly is proposed in this study. The effect of the shrink-fit interface contact is modelled as a contact force acted on rotor-AMBs system by applying distributed spring elements. We consider that there is partial separation in the contact interface due to the AMB levitating forces and a novel contact force model related to the contact status is developed by calculating the real-time contact area. The contact stiffness is determined based on the fractal model and fractal parameters are identified by experimental measured microscopic topography. The influences of the shrink-fit interference and the contact length on system response and stability is studied quantitatively through numerical simulation and experiment validation.

The main contributions of this work are:

(1) The combination of mechatronic model and the microscopic contact model. Based on the finite element-microscopic contact model, contact effect of shrink fit is considered as disturbance caused by the levitating forces and shrink-fit contact stiffness;
(2) Proposing a new contact force model, considering the change of contact state due to the levitating force;
(3) Investigating the influence of shrink-fit interference and the contact length on the system response and its stability by numerical simulation and experiment validation;
(4) Proposing a stable region using combinations of shrink-fit parameters on the assembly conditions based on the results of stability analysis.

After this introduction, the experimental system studied will be presented, then we will introduce the modelling of a rotor-AMBs system and the shrink-fit assembly (with contact stiffness model) will be presented. In Section 4, the identification of contact interface properties, numerical simulation and experimental validation will be discussed. the system stability will be then analyzed. The recommendations and conclusions will be addressed at the end.

2. Description of the system studied

The test rig is constituted with a steel shaft of 1.004 m length and 46 mm of diameter for a total weight of 10.35 kg (Fig. 1). It is supported by two identical AMBs powered in differential driving mode, with 8 poles and the action lines are positioned in the configuration load between axes. The bias current is 1.7 A and 0.25 mm for the air gap. Each AMB is supplied with a touch down bearings (TDBs) with 0.125 mm air gap, and two non-colocalized eddy current sensors. The AMBs are designed to generate a maximum dynamic force of 412 N. The AMB located in the middle is used as an Electro-Magnetic Actuator (EMA) and was not activated in this work and did not generate force. For the needs of this study, a shrink-fitted disk is assembled at the non-drive end. Since the study is carried out only during levitation, the rotor is not connected to the motor.

A PID (proportional-integral-derivative) controller is designed to stabilize the rotor-AMBs system and implemented on the dSPACE platform (DS1202, sampling frequency is 10 k Hz). An amplifier is used with 0.4 gain and 800 Hz cut- off frequency. AMBs, sensors and amplifier were designed and manufactured in the lab.

In order to assess the influence of interference and contact length, several aluminum alloy disks with a fixed outer diameter (D_{ro} = 16.008 mm) and different inner diameters D_{di} and different thickness L_d are manufactured by high-precision grinding machine (Fig. 2a). The inner diameters are measured by using an aperture tool with a measurement accuracy of 1 μm (Fig. 2b). The shrink-fit interference is 4, 5.5, 6.5, 7.5 and 9 μm. The contact length L_s is equaled disk's thickness, we can manufacture the disk with different contact lengths. Due to experimental limits, we manufactured the disks of the contact length within the range from 2 mm to 4 mm. The aim of the experiment using these disks is to assess the accuracy of the model and to predict the system response. To reduce the cost, we consider the contact lengths of 2, 3, and 4 mm in the experimental part.

Firstly, in order to identify which mode was affected by the shrink fit, the natural frequencies of the rotor were identified by using

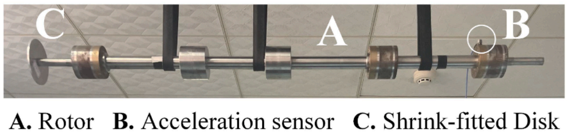

Fig. 3. Modal testing layout.

Table 1
Rotor bending natural frequencies.

Bending modes	Frequency (Hz): 2 mm disk thickness	Frequency (Hz): 3 mm disk thickness	Frequency (Hz): 4 mm disk thickness
1	93.08	92.69	92.23
2	261.59	260.32	258.89
3	534.69	531.32	525.65
4	947.02	861.72	857.87

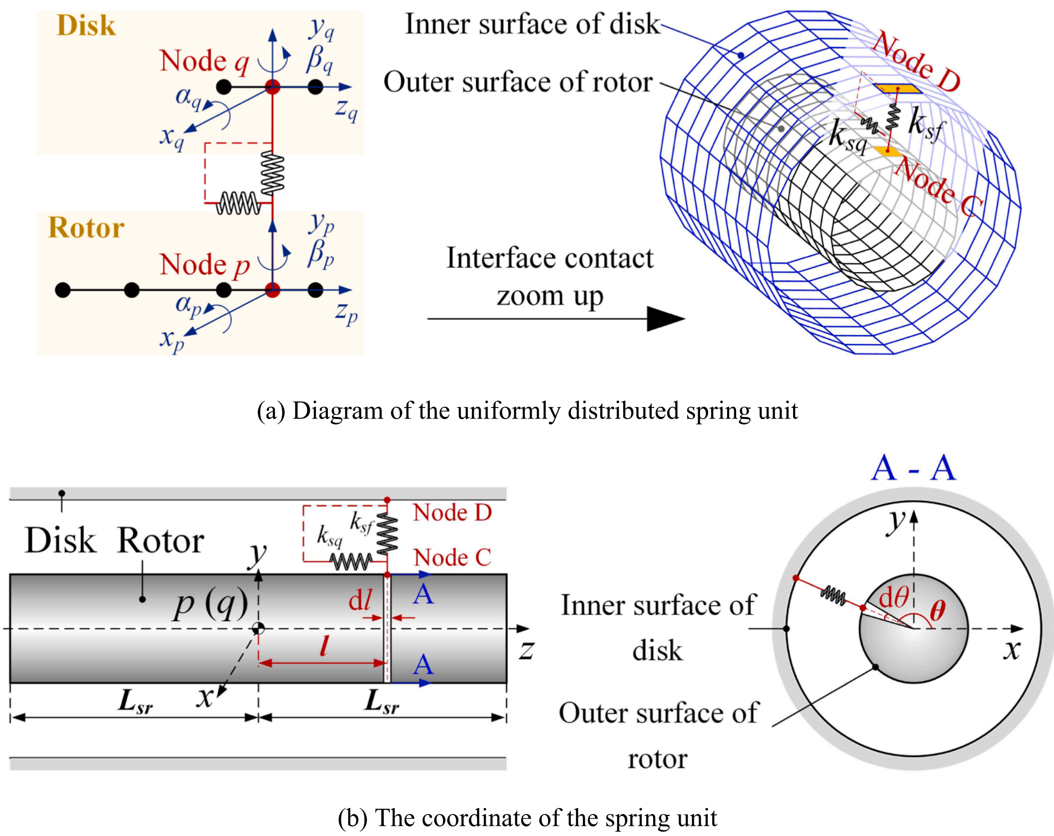

Fig. 4. Schematic diagram of the interface contact model formed by shrink fit.

modal testing. The rotor was suspended with three flexible tapes. An acceleration (PCB 352C65) was fixed on the laminations of AMB B (Fig. 3). The rotor was impacted at different position with an impact hammer (PCB 086C01).

The measured forces and accelerations for each impact was then processed by using OROS-36 data acquisition and signal processing system. The sampling frequency was 51.2 kHz that cover largely the frequency band studied. The results obtained for several disk thickness and for a fixed interference of 6.5 μm radial interference are presented in Table 1.

Form the results obtained, the most affected mode is 4th bending mode. When increasing the disk thickness from 3 mm to 4 mm, it has no significant effects. We did not make higher thickness since they were difficult to be assembled.

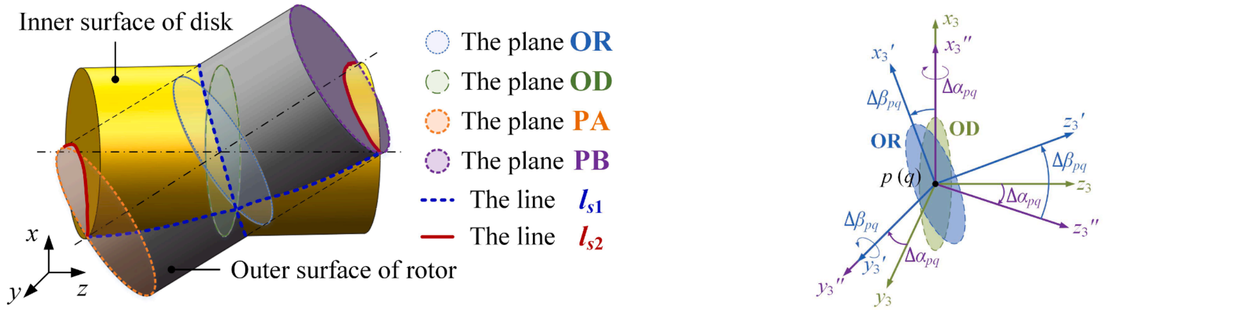

(a) Diagram of the partly separation in 3D view (b) Expansion of outer surface along circumferential direction

Fig. 5. Schematic diagram of the actual contact status between the rotor and the disk.

3. Modelling of rotor-AMBs system considering shrink fit interface contact

The modelling approach of the interface contact formed by the shrink-fit assembly will be presented first, then the rotor-AMBs system model will be describe.

3.1. Shrink fit interface contact model

The interface contact in the rotor is modeled as a uniformly distributed stiffness over the contact interface as shown in Fig. 4(a), where the disk and the rotor are joined together by shrink fit assembly. Each node in the outer surface of rotor (Node C) is connected to its corresponding node in the inner surface of disk (Node D) by the spring unit. The stiffness of the massless spring unit is referred to as the contact stiffness. The contact stiffness can be subdivided into the normal contact stiffness k_{sf} and the tangential contact stiffness k_{sq}. The directions of k_{sf} and k_{sq} are perpendicular and parallel to the contact interface, respectively.

There is relative displacement between the contact interfaces when the rotor vibrates. The energy generated by the spring deformation is calculated according to the energy principle of a spring unit Δu that can be obtained by the linear superposition of the change of the spring potential energy in the x ,y and z directions as:

$$\Delta u = \Delta u_x + \Delta u_y + \Delta u_z = \frac{1}{2}\cdot k_{sf}\Delta x^2 + \frac{1}{2}\cdot k_{sf}\Delta y^2 + \frac{1}{2}\cdot k_{sq}\Delta z^2 \tag{1}$$

where Δx, Δy and Δz represent the deformation of the spring unit in the x ,y and z directions, respectively.

In the shrink fit assembly, the center node of the rotor is node p and the center node of the disk is node q. The generalized coordinates of centers p and q are (x_p,y_p,α_p,β_p,z_p) and (x_q,y_q,α_q,β_q,z_q), respectively in absolute coordinates o-xyz. x ,y, z are the translations, α, β are the rotations. The subscript p is for node p, and q is for node q (Fig. 4).

By establishing the floating coordinate of node p and node q as shown in Fig. 4(b), Δx^2, Δy^2 and Δz^2 are obtained in the absolute coordinate system $oxyz$ as Appendix A.

The total energy U_s generated by the spring unit is obtained by summing up the unit spring energy Δu as follows

$$\begin{aligned} U_s &= \iint_A \frac{1}{2}\left(k_{sf}\Delta x^2 + k_{sf}\Delta y^2 + k_{sq}\Delta z^2\right)\mathrm{dA} = \int_{-L_{sr}}^{L_{sr}}\mathrm{d}l\int_0^{2\pi}\frac{1}{2}\left(k_{sf}\Delta x^2 + k_{sf}\Delta y^2 + k_{sq}\Delta z^2\right)R_s\mathrm{d}\theta \\ &= 2\pi R_s L_{sr} k_{sf}\left[\left(x_q - x_p\right)^2 + \left(y_q - y_p\right)^2\right] + \left(\frac{2}{3}\pi R_s L_{sr}^3 k_{sf} + \pi R_s^3 L_{sr} k_{sq}\right)\left[\left(\alpha_q - \alpha_p\right)^2 + \left(\beta_q - \beta_p\right)^2\right] \end{aligned} \tag{2}$$

where R_s is the nominal radius of the shrink-fit contact and L_s is the shrink-fit contact length ($L_s = 2L_{sr}$). A denotes the contact region, when the two interfaces are fully in contact, its area is given by $A_a = 2\pi R_s L_s$. The total energy U_s can be transformed as Eq. (3). According to the Lagrange equation, the contact stiffness can be obtained [2425].

$$U_s = \frac{1}{2}\begin{bmatrix} q_p \\ q_q \end{bmatrix}^{\mathrm{T}} K_{Es}\begin{bmatrix} q_p \\ q_q \end{bmatrix}, K_{Es} = \begin{bmatrix} \mathrm{diag}(vc \quad vc \quad vd \quad vd) & -\mathrm{diag}(vc \quad vc \quad vd \quad vd) \\ -\mathrm{diag}(vc \quad vc \quad vd \quad vd) & \mathrm{diag}(vc \quad vc \quad vd \quad vd) \end{bmatrix} \tag{3}$$

where $v_c = 4k_{sf}\bullet\pi R_s L_{sr}$, $v_d = 4k_{sf}\,\pi R_s L_{sr}{}^3/3 + 2k_{sq}\bullet\pi R_s{}^3 L_{sr}$, K_{Es} is the equivalent contact stiffness matrix, q_p is $(x_p,y_p,\alpha_p,\beta_p)^{\mathrm{T}}$, q_q is $(x_q, y_q,\alpha_q,\beta_q)^{\mathrm{T}}$.

The force vector F_{sc} generated by the interface can be obtained by calculating the partial derivative of the energy U_s with respect to the variable Δx_{qp} ($\Delta x_{qp} = x_q$-x_p), Δy_{qp} ($\Delta y_{qp} = y_q$-y_p), $\Delta\alpha_{qp}$ ($\Delta\alpha_{qp} = \alpha_q$-$\alpha_p$), $\Delta\beta_{qp}$ ($\Delta\beta_{qp} = \beta_q$-$\beta_p$)

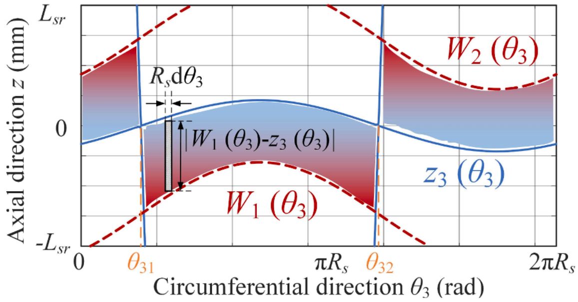

Fig. 6. Schematic diagram of the actual contact status between the rotor and the disk.

$$F_{sc} = \begin{bmatrix} \partial U_s/\partial \Delta x_{qp} \\ \partial U_s/\partial \Delta y_{qp} \\ \partial U_s/\partial \Delta \alpha_{qp} \\ \partial U_s/\partial \Delta \beta_{qp} \end{bmatrix} = \begin{bmatrix} F_{sx} \\ F_{sy} \\ F_{s\alpha} \\ F_{s\beta} \end{bmatrix} = \begin{bmatrix} k_{sf}\iint_A \mathrm{dA}\cdot \Delta x_{qp} \\ k_{sf}\iint_A \mathrm{dA}\cdot \Delta y_{qp} \\ \iint_A \left(k_{sf}l^2 + k_{sq}R_s^2\sin^2\theta\right)\mathrm{dA}\cdot \Delta\alpha_{qp} \\ \iint_A \left(k_{sf}l^2 + k_{sq}R_s^2\cos^2\theta\right)\mathrm{dA}\cdot \Delta\beta_{qp} \end{bmatrix} = \begin{bmatrix} Ks_x\left(q_p, q_q\right)\cdot \Delta x_{qp} \\ Ks_y\left(q_p, q_q\right)\cdot \Delta y_{qp} \\ Ks_\alpha\left(q_p, q_q\right)\cdot \Delta \alpha_{qp} \\ Ks_\beta\left(q_p, q_q\right)\cdot \Delta \beta_{qp} \end{bmatrix}$$
$$= \mathrm{diag}\left[Ks_x \quad Ks_y \quad Ks_\alpha \quad Ks_\beta\right]\cdot\left[\mathrm{diag}(-1) \quad \mathrm{diag}(1)\right]\cdot T_e q_r = Ks\cdot T_e q_r \tag{4}$$

where the value of Ks_x, Ks_y, Ks_α, Ks_β are all related to q_p and q_q.

However, the rotor and disk interfaces are not fully contacted during levitation and the contact region varies with rotor displacements at the contact surfaces [141626]. Thus, the integral domain in Eq. (4) is time-variant. It is assumed that the contact interface is partly separated as shown in Fig. 5. The blue line l_{s1} is formed by the intersection of the outer surface of the rotor and the inner surface of the disk. And the red lines l_{s2} are the lines formed by the intersection of the end faces of the rotor and the inner surface of the disk. The contact surface is divided into contact region and separated region by these lines. As shown in Fig. 6, we expand the rotor outer surface along the circumferential direction. The contact region is enclosed by $z_3(\theta_3)$ (the line l_{s1} function) and $W_1(\theta_3)$, $W_2(\theta_3)$ (line l_{s2} functions). The variables Ks_x, Ks_y, Ks_α, Ks_β can be expressed as

$$\begin{cases} Ks_x\left(q_p, q_q\right) = \int_{W_1(\theta_3)}^{z_3(\theta_3)}\int_{\theta_{31}}^{\theta_{32}} k_{sf}R_s\mathrm{d}\theta_3\mathrm{dl} + \int_{z_3(\theta_3)}^{W_2(\theta_3)}\int_{\theta_{32}}^{\theta_{31}+2\pi} k_{sf}R_s\mathrm{d}\theta_3\mathrm{dl} \\ Ks_y\left(q_p, q_q\right) = \int_{W_1(\theta_3)}^{z_3(\theta_3)}\int_{\theta_{31}}^{\theta_{32}} k_{sf}R_s\mathrm{d}\theta_3\mathrm{dl} + \int_{z_3(\theta_3)}^{W_2(\theta_3)}\int_{\theta_{32}}^{\theta_{31}+2\pi} k_{sf}R_s\mathrm{d}\theta_3\mathrm{dl} \\ Ks_\alpha\left(q_p, q_q\right) = \int_{W_1(\theta_3)}^{z_3(\theta_3)}\int_{\theta_{31}}^{\theta_{32}} \left(k_{sf}l^2 + k_{sq}R_s^2\sin^2\theta_3\right)R_s\mathrm{d}\theta_3\mathrm{dl} + \int_{z_3(\theta_3)}^{W_2(\theta_3)}\int_{\theta_{32}}^{\theta_{31}+2\pi} \left(k_{sf}l^2 + k_{sq}R_s^2\sin^2\theta_3\right)R_s\mathrm{d}\theta_3\mathrm{dl} \\ Ks_\beta\left(q_p, q_q\right) = \int_{W_1(\theta_3)}^{z_3(\theta_3)}\int_{\theta_{31}}^{\theta_{32}} \left(k_{sf}l^2 + k_{sq}R_s^2\cos^2\theta_3\right)R_s\mathrm{d}\theta_3\mathrm{dl} + \int_{z_3(\theta_3)}^{W_2(\theta_3)}\int_{\theta_{32}}^{\theta_{31}+2\pi} \left(k_{sf}l^2 + k_{sq}R_s^2\cos^2\theta_3\right)R_s\mathrm{d}\theta_3\mathrm{dl} \end{cases} \tag{5}$$

We need to know $W_1(\theta_3)$, $W_2(\theta_3)$ and $z_3(\theta_3)$ to calculate the contact force. The details can be seen in Appendix B and C.

3.2. Calculation of the normal and the tangential stiffness

The contact stiffness model of shrink-fit interfaces is established based on the elastic–plastic contact model. It enables the determination of the relationships among contact stiffness, the contact length and the shrink-fit interference.

3.2.1. Shrink-fit microscopic contact model

According to [21], the pressure produced by the shrink fit can be calculated as follows

$$P_c = \frac{\delta_c}{R_s\left[\frac{1}{E_d}\left(\frac{R_{do}^2+R_s^2}{R_{do}^2-R_s^2}+\nu_d\right)+\frac{1}{E_r}\left(\frac{R_s^2+R_{ri}^2}{R_s^2-R_{ri}^2}-\nu_r\right)\right]} \tag{6}$$

where P_c is the shrink-fit pressure, E_d and E_r are respectively the Young modulus of the disk and the rotor, the υ_d and υ_r are respectively the Poisson's ratio of the disk and the rotor, the δ_c is the static interference of the shrink-fit assembly, the R_{do} is the disk's outer radius ($D_{do}/2$), the R_{ri} is the inner radius of the rotor ($D_{ri}/2$).

The normal load F_n of the contact surface can be expressed as

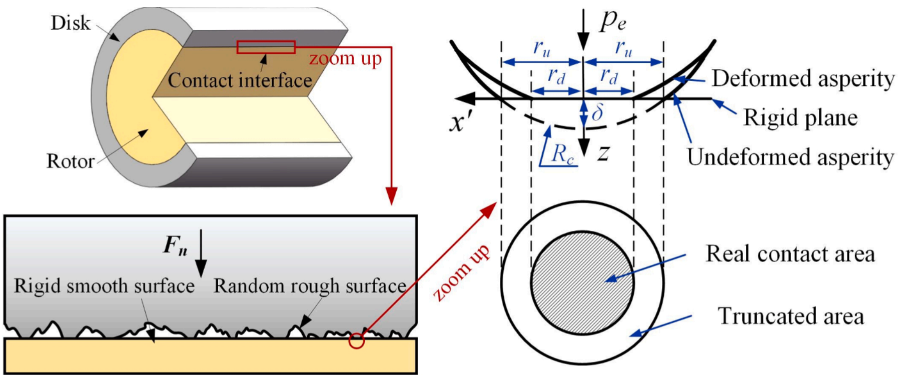

Fig. 7. Schematic diagram of the contact surface, and the deformation geometry of an individual asperity.

$$F_n = P_c \times A_a = 2\pi R_s L_s P_c \tag{7}$$

A graphical representation of the simplified contact and the deformation geometry of an individual asperity is given in Fig. 7., the contact behavior of two rough surfaces (rotor and disk contact interfaces) can be simplified as the contact of an equivalent rough surface and a rigid surface.

The fractal theory is used to describe the random features of the contact interface, facilitating the calculation of the normal and tangential contact stiffness based on contact theory. According to [27], the two-dimensional rough surface profile can be described by the improved Weierstrass-Mandelbrot (W-M) function as

$$z_1(x') = L(G/L)^{D-1}(\ln 1.5)^{0.5}\sum_{i=0}^{i_{\max}} 1.5^{(D-2)n}\left[\cos\phi_{1,i} - \cos\left(2\pi\cdot 1.5^n x'/L - \phi_{1,i}\right)\right] \tag{8}$$

where $z_1(x')$ is the rough surface height and x is the lateral distance, D is the fractal dimension ($1 < D < 2$) and G is the fractal roughness, L represents the sample length of surface profile, i is the frequency index and $i_{\max}$ corresponds to the high cutoff frequency of the profile, $\phi_{1,i}$ denotes the phase that is chosen randomly, and x' is the coordinate along the surface. The deformation of an individual asperity can be expressed as

$$\delta = 2G^{D-1}(\ln 1.5)^{0.5}(2r_u)^{2-D} \tag{9}$$

where r_u is the truncated radius of the undeformed asperity (Fig. 7).

According to the deformation geometry of an individual asperity, the relationship between δ and r_u is given by R_c^2- $(R_c^2$-$\delta^2) = r_u^2 = a_u/\pi$ and $R_c \gg \delta$, in which a_u is the truncated area of the microcontact. The radius of the curvature of the microcontact can be derived as

$$R_c = 2^{D-4}G^{1-D}(\ln 1.5)^{-0.5}(a_u/\pi)^{0.5D} \tag{10}$$

The asperities of the rough surface with different heights will generally be in two deformation states: fully elastic deformations and fully plastic deformations. Based on Hertz contact theory, the relationship between normal contact load p_e and the local normal deformation δ for a single microcontact in elastic contact regime can be expressed as

$$p_e(a_u) = \frac{4}{3}\overline{E}R_c^{0.5}\delta^{1.5} = \frac{2^{4.5-D}}{3\pi^{1.5-0.5D}}\overline{E}G^{D-1}(\ln 1.5)^{0.5}(a_u)^{1.5-0.5D} \tag{11}$$

where $\overline{E}$ is the equivalent elastic modulus, $1/\overline{E}=(1\text{-}\nu_r^2)/E_r+(1\text{-}\nu_d^2)/E_d$.

The normal contact load of a single microcontact with plastic deformation can be expressed as

$$p_p(a_u) = 2.8\sigma_s a_u \tag{12}$$

where σ_s is the yield strength of the disk material.

According to [28], the size distribution function $n(a_u)$ of microcontacts is given by

$$n(a_u) = 0.5D\psi^{1-0.5D}a_{ul}^{0.5D}a_u^{-0.5D-1} \tag{13}$$

where a_{ul} represents the maximum truncated area of the microcontact. The domain extension factor ψ can be calculated based on the following equation,

$$\left(1+\psi^{-0.5D}\right)^{(D-2)/D} = (2-D)/D \tag{14}$$

To sum up, the relationship between the normal load of the shrink-fit assembly and the maximum real contact area a_{rl} of the microcontact is given by

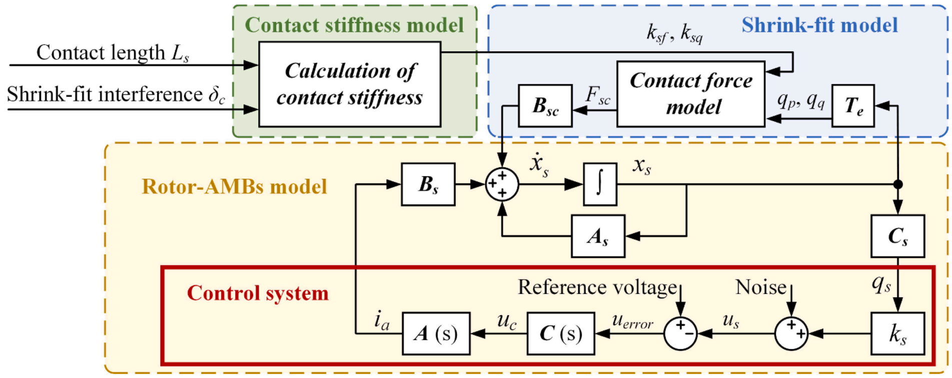

Fig. 8. Schematic diagram of the rotor-AMBs system considering shrink-fit interface contact.

$$\begin{aligned} F_n &= \int_{a_{uc}}^{a_{ul}} p_e(a_u)n(a_u)\mathrm{d}a_u + \int_0^{a_{uc}} p_p(a_u)n(a_u)\mathrm{d}a_u \\ &= \frac{2^{6-1.5D}D\overline{E}(\ln 1.5)^{0.5}G^{D-1}\psi^{1-0.5D}}{3\pi^{1.5-0.5D}(3-2D)}a_{rl}^{0.5D}\left[a_{rl}^{1.5-D}-a_{rc}^{1.5-D}\right] + \frac{2k\sigma_s D\psi^{1-0.5D}}{2-D}a_{rl}^{0.5D}a_{rc}^{1-0.5D} \end{aligned} \tag{15}$$

where a_{rc} represents the critical real contact area demarcating the elastic and plastic regimes, given by $a_{rc} = G^2/(1.4\sigma_s/\overline{\mathrm{E}})^{2/(D-1)}$. By Hertz contact theory, the critical truncated contact area a_{uc} is determined by $a_{uc} = 2\pi R_c\delta_{uc}$ and the relationship between a_{uc} and the real critical contact area a_{rc} can be concluded as $a_{uc} = 2a_{rc}$. On the other hand, the maximum real contact area a_{rl} can be expressed as $a_{rl} =$ (2-D)$\psi^{0.5D-1}A_{rc}/D$, where A_{rc} is the real contact area of the contact surface. Likewise, the relationship between a_{rl} and the maximum truncated contact area a_{ul} is given as $a_{ul} = 2a_{rl}$.

With F_n calculated earlier, we can obtain the maximum real contact area a_{rl} from Eq. (15). This step is to obtain the real contact area distribution, which will be used to determine the distributions of contact stiffness.

3.2.2. Shrink-fit contact stiffness model

The total contact stiffness is determined by integrating the stiffness of each interacting microcontact with the size distribution function of microcontacts shown in Fig. 7. By differentiating Eq. (11), the normal contact stiffness for a single microcontact in contact with a rigid plane could be written as

$$k_n = \frac{\mathrm{d}p_e}{\mathrm{d}\delta} = \left(\frac{2a_u}{\pi}\right)^{0.5}\overline{E} \tag{16}$$

Thus, the total normal contact stiffness is given by

$$K_n = \int_{a_{uc}}^{a_{ul}} k_n n(a_u)\mathrm{d}a_u = \frac{2D\overline{E}}{\pi^{0.5}(1-D)}\psi^{1-0.5D}a_{rl}^{0.5D}\left[a_{rl}^{0.5-0.5D}-a_{rc}^{0.5-0.5D}\right] \tag{17}$$

The equivalent elastic deformation in the tangential direction for a single micro-contact interacting with a rigid plane is

$$\tau = \frac{3\mu f_n}{16\overline{G}(a_u/2\pi)^{0.5}}\left[1-(1-f_t/\mu f_n)^{2/3}\right] \tag{18}$$

where f_n and f_t represent the normal and tangential contact loads acting on a single microcontact, $\overline{\mathrm{G}}$ is the equivalent shear modulus, $1/\overline{\mathrm{G}}$=(2-ν_r)/G_r+(2-ν_d)/G_d, G_r and G_d are the shear moduli of the rotor and disk, respectively, and μ denotes the friction coefficient. By differentiating Eq. (18), the tangential contact stiffness for a single microcontact interacting with a rigid plane is given by

$$k_t = \frac{\mathrm{d}f_t}{\mathrm{d}\tau} = 4\cdot\left(\frac{2a_u}{\pi}\right)^{0.5}\overline{G}\left(1-\frac{f_t}{f_n\mu}\right)^{\frac{1}{3}} \tag{19}$$

Thus, the total tangential contact stiffness is given by

$$K_t = \int_{a_{uc}}^{a_{ul}} k_t n(a_u)\mathrm{d}a_u = \frac{8D\overline{G}}{\pi^{0.5}(1-D)}\psi^{1-0.5D}a_{rl}^{0.5D}\left[a_{rl}^{0.5-0.5D}-a_{rc}^{0.5-0.5D}\right] \tag{20}$$

Assuming that the normal and tangential stiffness are uniformly distributed over the contact interface, the stiffness of each spring unit can be expressed as

$$\begin{cases} k_{sf} = K_n/A_a = K_n/2\pi R_s L_s \\ k_{sq} = K_t/A_a = K_t/2\pi R_s L_s \end{cases} \tag{21}$$

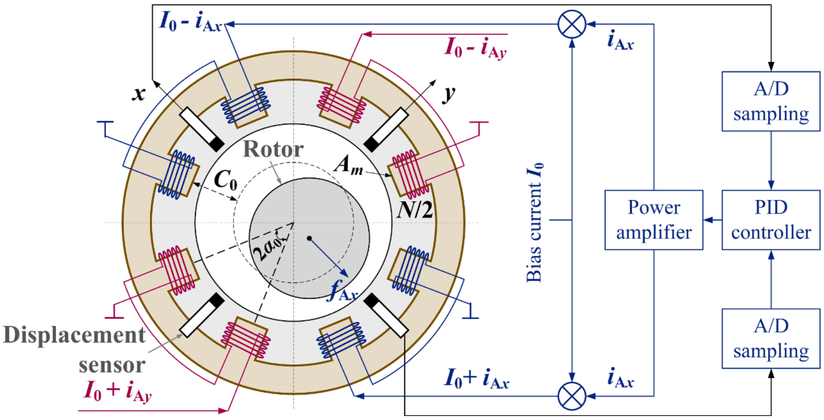

Fig. 9. Structure and principle of a radial AMB.

3.3. Rotor-AMBs model

The model of rotor-AMBs system considering interface contact consists of three parts as shown in Fig. 8: the contact stiffness model, the shrink-fit model and the rotor-AMBs model. In section 3.1, the effect of shrink-fit interface contact is modelled as the contact force F_{sc} acted on the rotor-AMBs model. In section 3.2, the shrink-fit contact stiffness applied in shrink-fit model is calculated under different contact length L_s and shrink-fit interference δ_c based on the microscopic contact model. In section 3.3, the rotor-AMBs model is established based on previous work.

Finite element method is used. The shaft is modeled with 63 Bernoulli-Euler beam elements with two nodes and four degree of freedom (DOF) per node. Two radial translations and two associated rotations. The axial DOF is not considered in this study. The general equation of motion is obtained by applying Lagrange equation [29]. Based on Eq. (3) and Eq. (4), the contact stiffness matrix K_{Es} and contact force vector F_{sc} is then added:

$$M_R\ddot{q}_r + C_R\dot{q}_r + \left(K_R + T_e{}^T K_{Es} T_e\right)q_r = T_a{}^T F_{AMB} + T_{sc}{}^T F_{sc} \tag{22}$$

where M_R, C_R and K_R are the mass, damping and stiffness matrices of the system, respectively. q_r is the rotor displacement vector. The force vectors F_{AMB} represents the electromagnetic force by the AMBs A and B in the x and y directions, T_a is the transfer matrix of the AMB nodes, T_e is the transfer matrix of node p and node q, T_{sc} is the transfer matrix of node p.

AMBs are used to levitate the rotor and the Fig. 9 recalls all the required electromechanical components (including the electromagnet, the power amplifier and the controller), to generate the attractive magnetic force f_{amb} along the action line. The control current i_a is provided by the controller according to the measured rotor relative displacement with respect to the center of AMBs. According to the fundamental formula of the electromagnetic force [1], f_{amb} is linearized as

$$f_{amb} = \frac{\mu_0 A_m N_c^2 \cos\alpha_0}{4}\left[\left(\frac{I_0 + i_a}{C_0 - x\cos\alpha_0}\right)^2 - \left(\frac{I_0 - i_a}{C_0 + x\cos\alpha_0}\right)^2\right] \approx \frac{\mu_0 A_m N_c^2 I_0^2 \cos^2\alpha}{C_0^3}x + \frac{\mu_0 A_m N_c^2 I_0 \cos\alpha}{C_0^2}i_a = k_h x + k_i i_a \tag{23}$$

where μ_0 the permeability of vacuum, A_m the area of one pole, N_c the turns per coil of a pair of poles, C_0 the radial air gap, $x\cos\alpha_0$ the actual variation of the air gap in the x direction. k_h and k_i the displacement and the current stiffness, respectively.

The eddy current sensors are modelled as the proportional component which transform the displacement to voltage, and the gain of sensor model is k_s.

The amplifier transfer function has been verified by experimental results and is expressed as [1]:

$$A(s) = \frac{k_a(2\pi f_z)}{s + (2\pi f_z)} \tag{24}$$

where k_a is the gain of power amplifier, f_z is the cut-off frequency.

In this work, a PID controller is used to ensure stable levitation of the rotor, it has the transfer function of

$$C(s) = K_P + \frac{K_I}{s} + \frac{K_D s}{T_D s + 1} \tag{25}$$

where K_P, K_I and K_D respectively represents the proportional, the integral and the derivative gains, T_D is the derivative time constant to prevent magnifying the error signal by the controller in the high frequency ranges.

Substituting Eq. (23) into Eq. (22), the state space model of the rotor-AMBs system considering the interface contact can be expressed as Eq. (26) by taking $\{x_s\} = [\mathrm{q_r}\ \dot{\mathrm{q}}_\mathrm{r}]^\mathrm{T}$.

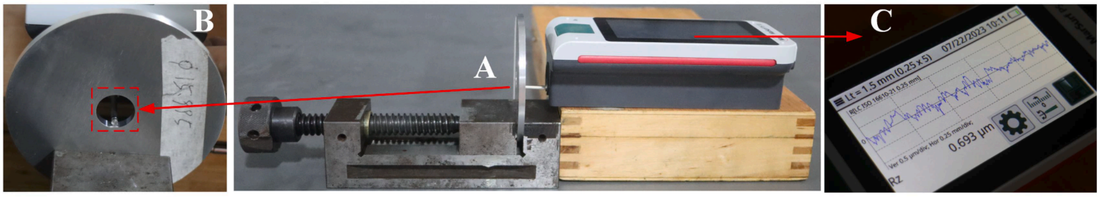

A. Roughness measuring instrument **B.** Surface to be measured **C.** Data processing software

Fig. 10. Disposition for the surface profile measurement.

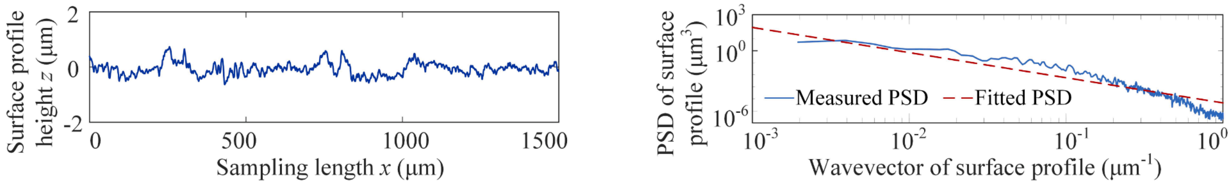

(a) Surface profile height curves (b) Measured and fitted PSD curve

Fig. 11. Measurement and parameters estimation. (Ld = 4 mm, Ddi = 15.995 mm).

$$
\begin{cases} \{\dot{x}_s\} = [A_s]\{x_s\} + [B_s]i_a + [B_{sc}]F_{sc} \\ \{q_s\} = [C_s]\{x_s\} \end{cases}
$$

$$
[A_s] = \begin{bmatrix} 0_{256\times256} & I_{256\times256} \\ M_R^{-1}\left(k_h T_a^T T_a - K_R - T_e^T K_{Es} T_e\right) & -M_R^{-1}C_R \end{bmatrix}; [B_s] = \begin{bmatrix} 0_{256\times4} \\ k_i M_R^{-1} T_a^T \end{bmatrix}; \ [B_{sc}] = \begin{bmatrix} 0_{256\times4} \\ M_R^{-1} T_{sc}^T \end{bmatrix};
$$

$$
[C_s] = [\, T_s \quad 0_{256\times4} \,] \tag{26}
$$

where $\{x_s\}$ is the state vector, q_s is the displacement of the sensor nodes in the x and y directions, and T_s is the transfer matrix of the sensor nodes.

When the rotor is levitated stably, an external random excitation induced by the whole arrangement of electronic devices used, leading to micro vibrations with a maximum displacement amplitude is about 1 μm. The noise in the closed-loop is unavoidable in experimentation. Therefore, in the numerical simulation, white noise excitation is added to the feedback path.

4. Results

Experiments were done in order to estimate the shrink fit parameters. Then results stemming from numerical simulation and experiments were compared in order to validate the model developed. Experiments and numerical simulations were performed with the same conditions: for a given parameter for the shrink fit (shrink-fit interference δ_c and contact length L_s), levitate the rotor by using the AMBs and inducing white noise exciting to simulate the electronic noise observed experimentally. Once the model developed was validated, the stability analysis could be performed.

4.1. *Shrink-fit parameters estimation and validation*

To obtain the accurate relationship between contact stiffness, shrink-fit interference and contact length, it is necessary to estimate the fractal dimension D and the fractal roughness G. These two fractal parameters are identified based on the PSD (Power Spectral Density) function [30]. The PSD of the surface profile can be expressed as

$$
\log P(\omega_p) = (2D-5)\log(\omega_p) + (2D-2)\log G - \log(\ln 1.5) + (4-2D)\log\pi + (3-2D)\log 2 \tag{27}
$$

where P denotes the PSD and ω_p is the wavevector of surface profile.

The inner surface topography is measured using a roughness measuring instrument (MarSurf PS 10) shown in Fig. 10. The surface profile height of disk's inner surface was measured (Fig. 11(a)). The PSD evolution along the contact surface was obtained by using the least square curve fitting method (Fig. 11(b)).

The different values of the fractal dimension and the fractal roughness obtained are presented in Appendix D. For the numerical simulation, the average values were used: 1.454 for D and 0.973×10^{-10} m for G. The normal and the tangential contact stiffness are then calculated (presented in Appendix E). It can be noticed that the stiffness increases with the increase of the shrink-fit parameters (δ_c

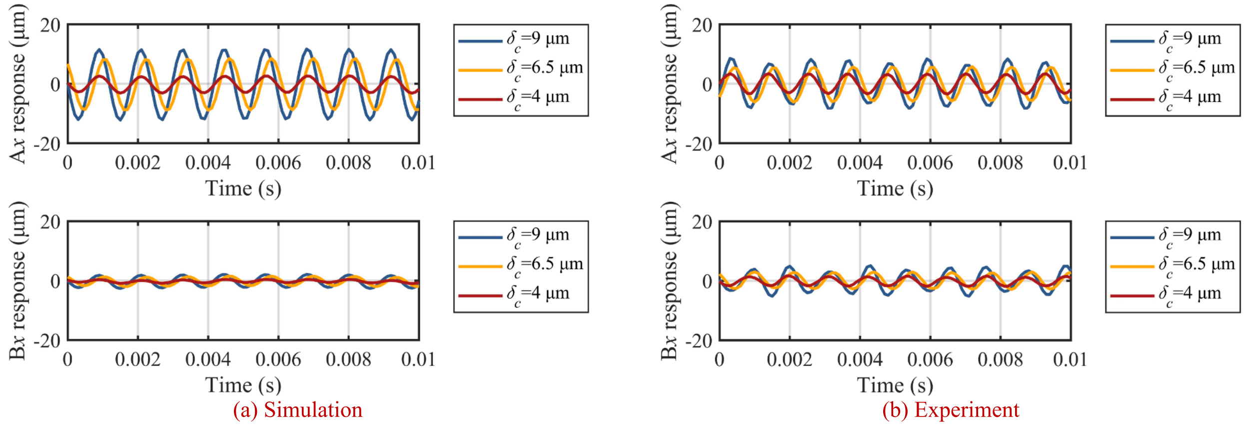

Fig. 12. Comparison of time-domain responses in simulation and experiment (different interferences).

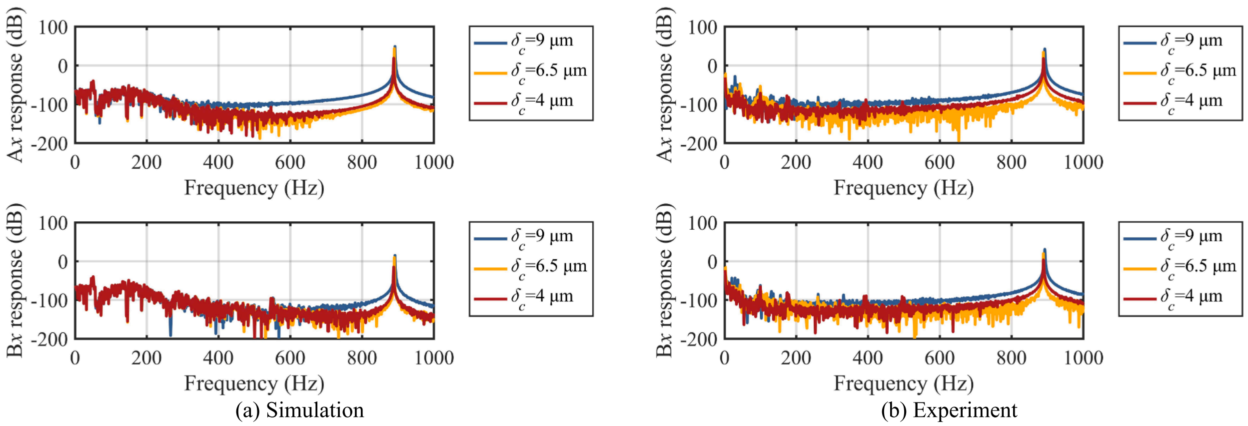

Fig. 13. Comparison of frequency-domain responses in simulation and experiment (different interferences).

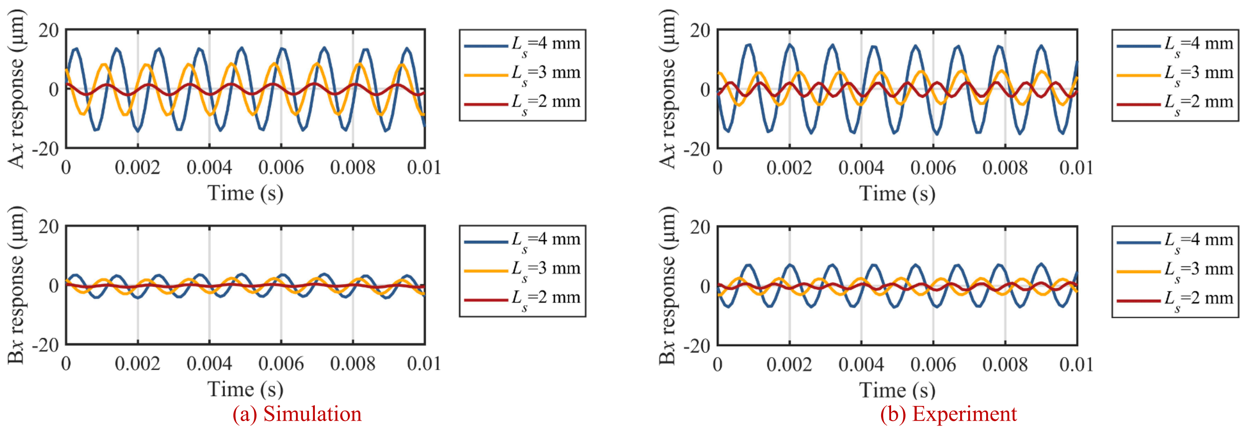

Fig. 14. Comparison of time-domain responses in simulation and experiment (different contact lengths).

and L_s). During the repetitions of shrink-fit assembly, the possible wear in contact surfaces may be caused which results in the uncertainty of the shrink-fit estimation. Several repeated experiments were done to check the influence of uncertainty on shrink-fit estimation. The relative errors were small and the maximum relative error of 0.14 % in fractal dimension and of 3.49 % in fractal roughness were observed. The uncertainty in the identification of shrink-fit fractal parameters has little influence on the calculation of contact stiffness.

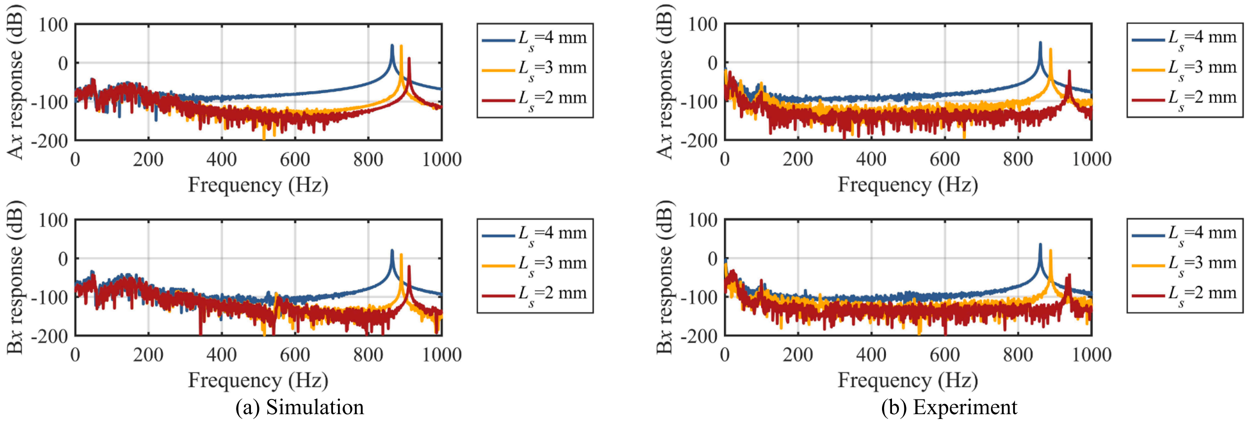

Fig. 15. Comparison of frequency-domain responses in simulation and experiment (different contact lengths).

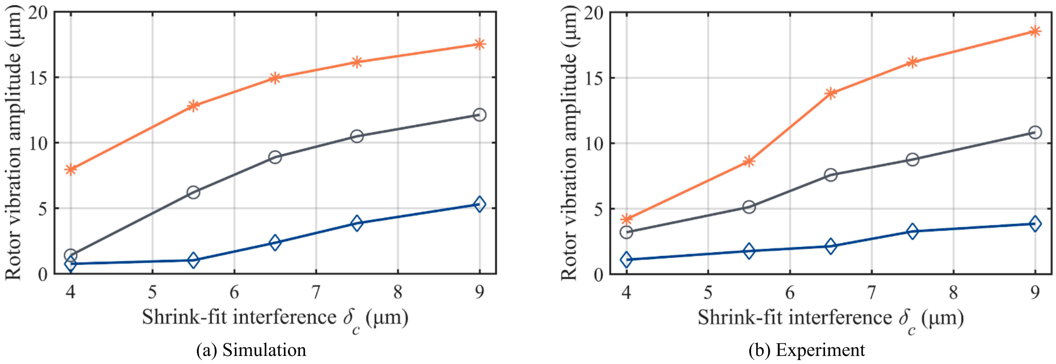

Fig. 16. Comparison of the vibration amplitude at the position of AMB A (different shrink-fit interferences and contact lengths).

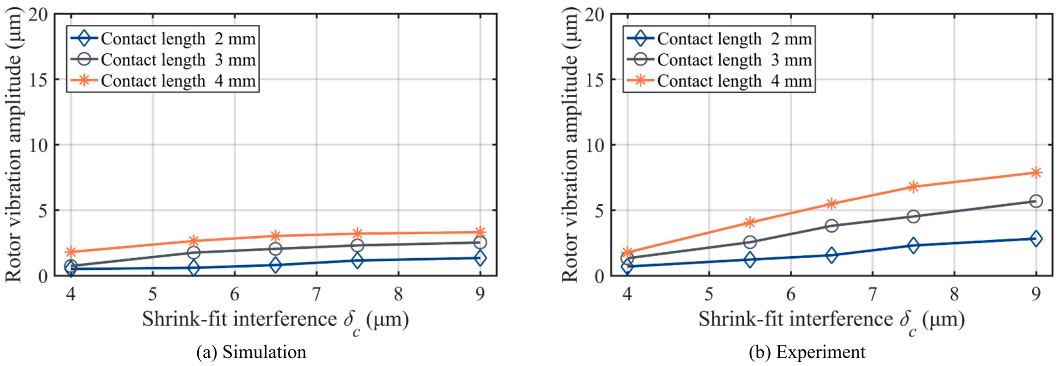

Fig. 17. Comparison of the vibration amplitude at the position of AMB B (different shrink-fit interferences and contact lengths).

4.2. Dynamic analysis and model validation

To study the influence of the shrink fit parameters on the system, appropriate control parameters should be tuned to ensure stable levitation of the rotor without shrink-fit interface contact and these parameters will be kept the same during different experimental phases to exclude the influence of the controller (presented in Appendix D). The PID parameters were tuned experimentally. Same parameters were applied in numerical simulation. The identified values were: $K_P = 1.7$, $K_I = 1$, $K_D = 0.0006$, $T_D = 0.0001$. Same sampling frequency (10 kHz) was used in both, numerical simulation and experiments, which satisfies the standards recommendations of sampling frequency in rotor-AMBs system [31].

The displacement responses in time and frequency domain in x direction for both AMBs (A and B) are presented in Fig. 12 and Fig. 13 for the median value of L_s (3 mm) and different values of δ_c.

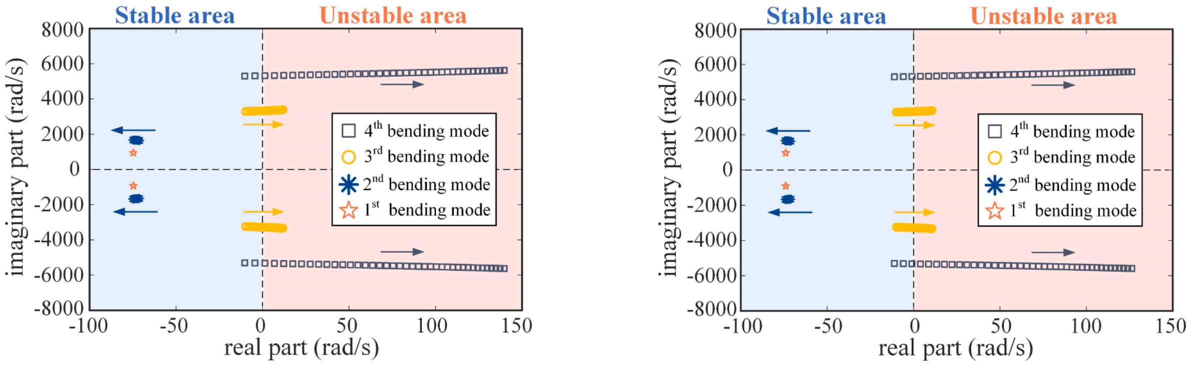

(a) Root locus for different shrink-fit interferences (0.2 to 20 μm) (b) Root locus for different contact lengths (0.2 to 8 mm)

Fig. 18. Root locus of the closed-loop system.

Same general trends are observed in both numerical simulations and experiments. The model developed describes closely the dynamic behavior of the system studied in the frequency range of interest. In this study, we are interested in the behavior around the 4th bending mode that presents instabilities. Similar behavior could be observed in both. The amplitude of the response increases as δ_c increases. The system model seems to be more damped. Same trends are observed in y direction.

When δ_c is 6.5 μm (the median value), varying L_s from 2 mm to 4 mm, the response amplitude of the 4th bending mode increases, as shown in Fig. 14 and Fig. 15. We can also observe that increasing L_s shifts the 4th bending mode frequency toward lower values and the energy induced by the interface contact has greater impact on the dynamic behavior near AMB A (near the shrink-fitted disk). Those observations should be considered when adjusting the controller parameters. Here also the model describes closely the behavior observed experimentally. Same trends are observed in the y direction.

To sum up, the amplitude of the response increases and the instability intensifies with the increase of δ_c and L_s. To further validate the reliability of the model developed, the theoretical and experimental rotor 4th bending mode amplitude under different shrink-fit interferences and contact lengths are shown in Fig. 16 and Fig. 17, respectively. Same general trends are observed numerically and experimentally. The difference between the vibration amplitude at AMB B is larger in experiment results, however the effect of shrink-fit has less influence at this position. It should be noted that, the aim of this study was to understand phenomena that induce the instability and to point out the parameters that influence these phenomena. We didn't try to adjust the model parameters to reproduce closely the vibration amplitudes, that will be done in the future. Due to several repetitive shrink-fit procedures made, there may be modifications and wear in the rotor surface (that we didn't quantify in this study). Small differences were observed for the different results measured.

4.3. Stability analysis

The root locus analysis is applied to study how the shrink-fit assembly influence the stability of rotor-AMBs system. Based on Eq. (4), the contact force can be expressed as $F_{sc} = K_s \bullet T_e \bullet q_r$. The control current can be expressed as $i_a = H_s \bullet q_s = H_s \bullet T_s \bullet q_r$. Consequently, the state space in Eq. (26) can be transformed as:

$$A_{sr} = \begin{bmatrix} 0 & I \\ M_R^{-1}\left(k_h T_a^{\mathrm{T}} T_a - K_R - T_e^{\mathrm{T}} K_{Es} T_e + k_i T_a^{\mathrm{T}} H_s T_s + T_{sc}^{\mathrm{T}} K_s T_e\right) & -M_R^{-1} C_R \end{bmatrix} \tag{28}$$

The closed-loop system eigenvalues λ can be calculated as:

$$\det(\lambda I - A_{sr}) = 0 \tag{29}$$

As A_{sr} is dependent on the shrink-fit interference and the contact length, therefore, different eigenvalues λ will result for the different combination of the shrink-fit parameters. The root locus of the eigenvalues for the different combinations studied were calculated (Fig. 18).

The root locus of the system closed-loop is calculated for the configuration the contact length 3 mm and for different values of δ_c (Fig. 18a). When no shrink-fit applied, all roots of the system are stable, and that what is observed experimentally. On the other hand, when applying the shrink-fit, it can be noticed that the roots for the first two bending modes still stable for different values of δ_c, but the roots for the 3rd and 4th modes move toward unstable locus. However, and as it can be seen on Fig. 15, the amplitude of the 3rd mode is too small to influence the stability of the system.

The root locus of the system closed-loop is also calculated for the configuration shrink-fit interference 3 mm and different contact length values (Fig. 18b). The same trends are observed.

It is obvious that to maintain the system stable, the controller should be able to mitigate the 4th bending mode over its frequency range variation.

Stemming from the root locus analysis, variables δ_c and L_s influence system stability. For further design optimization aiming at

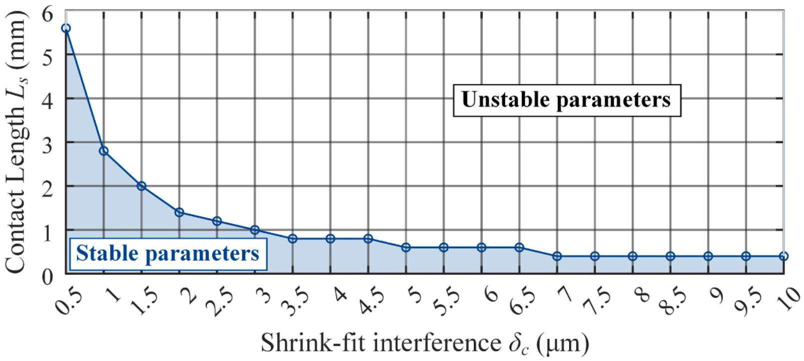

Fig. 19. Stable region as a function of shrink-fit parameters.

decreasing the influence of the shrink-fit interface contact, stable region can be obtained to guide the safe operation (Fig. 19). The stable parameter combinations of shrink-fit interference δ_c and contact length L_s are specified based on the real parts of the 4th bending mode roots.

5. Conclusions

The aim of this research work is to investigate numerically and experimentally the instability caused by shrink-fit interface contact in a rotor-AMBs system and to identify the parameters that influence this instability.

The instability is due to the relative displacement between the contact surfaces of rotor and disk when the rotor is levitated. The shrink-fit assembly introduces discontinuity in the contact and contact force arises from this relative displacement. Moreover, the rotor and the disk interfaces are not fully in contact when the rotor is levitated. The actual area of contact interface decreases with the increase of the vibration amplitude, resulting in the decrease of the contact force. The normal and the tangential contact stiffness were calculated by using the contact characteristics identified experimentally.

The unstable zones are identified as a function of the shrink-fit interference and the contact length. The influencing parameters were pointed out, and their effects on the system dynamic behavior was studied. Based on the simulation and experimental results under different shrink-fit interferences and contact lengths, the instability is induced by the effect of shrink-fit parameters on the roots of the 4th bending mode. From the stability analysis results, the increase of shrink-fit interference and the contact length, moves the roots of the 4th bending mode to the unstable zone and leads to an increase of the vibration amplitude. Increasing the contact length shifts the 4th bending mode frequency toward lower values, this fact should be considered when designing the controller in the future. Based on stability analysis results and reliable model, the stable parameter combinations of shrink-fit parameters are specified to guide the safe operation.

The model developed is able to reproduce the overall dynamics in the frequency range of interest and the main observed phenomenon which provides reliable prediction of the dynamic behavior of the studied system. This model will be used to conduct further investigations on the optimal design of the shrink-fit assembly and the developing of efficient robust controller to suppress this vibration.

CRediT authorship contribution statement

Yang Zhou: Writing – review & editing, Writing – original draft, Validation, Software, Methodology, Investigation, Formal analysis, Conceptualization. **Yuanping Xu:** Writing – review & editing, Validation, Resources, Methodology, Investigation. **Jin Zhou:** Supervision, Project administration, Methodology, Funding acquisition, Conceptualization. **Yue Zhang:** Writing – review & editing, Resources, Methodology, Conceptualization. **Jarir Mahfoud:** Writing – review & editing, Software, Methodology, Investigation, Formal analysis, Conceptualization.

Declaration of competing interest

The authors declare that they have no known competing financial interests or personal relationships that could have appeared to influence the work reported in this paper.

Data availability

Data will be made available on request.

Acknowledgment

This work was supported by the National Natural Science Foundation of China (52075239).

Appendix A

The coordinates of Node C and Node D can be expressed as in the absolute coordinate system *oxyz* as

$$\begin{cases} x_C = x_p + l\cdot \sin\alpha_p\cos\beta_p + R_s\cos\theta\cos\beta_p \\ y_C = y_p + l\cdot \sin\beta_p + R_s\cos\theta\sin\beta_p\sin\alpha_p + R_s\sin\theta\cos\alpha_p \\ z_C = z_p + l\cdot \cos\alpha_p\cos\beta_p - R_s\cos\theta\sin\beta_p\cos\alpha_p + R_s\sin\theta\sin\alpha_p \end{cases} \tag{A.1}$$

$$\begin{cases} x_D = x_q + l\cdot \sin\alpha_q\cos\beta_q + R_s\cos\theta\cos\beta_q \\ y_D = y_q + l\cdot \sin\beta_q + R_s\cos\theta\sin\beta_q\sin\alpha_q + R_s\sin\theta\cos\alpha_q \\ z_D = z_q + l\cdot \cos\alpha_q\cos\beta_q - R_s\cos\theta\sin\beta_q\cos\alpha_q + R_s\sin\theta\sin\alpha_q \end{cases} \tag{A.2}$$

The deformation of the spring unit Δx, Δy and Δz in the absolute coordinate system are calculated by the coordinates of node C and node D as,

$$\begin{cases} \Delta x = x_D - x_C \\ = x_q - x_p + l\left(\sin\alpha_q\cos\beta_q - \sin\alpha_p\cos\beta_p\right) + R_s\cos\theta\left(\cos\beta_q - \cos\beta_p\right) \\ \Delta y = y_D - y_C \\ = y_q - y_p + l\left(\sin\beta_q - \sin\beta_p\right) + R_s\cos\theta\left(\sin\alpha_q\sin\beta_q - \sin\alpha_p\sin\beta_p\right) + R_s\sin\theta\left(\cos\alpha_q - \cos\alpha_p\right) \\ \Delta z = z_D - z_C \\ = z_q - z_p + l\left(\cos\alpha_q\cos\beta_q - \cos\alpha_p\cos\beta_p\right) + R_s\cos\theta\left(\cos\alpha_p\sin\beta_p - \cos\alpha_q\sin\beta_q\right) + R_s\sin\theta\left(\sin\alpha_q - \sin\alpha_p\right) \end{cases} \tag{A.3}$$

Considering the first-order Taylor expansion of $\sin x$ is x , and the first-order Taylor expansion of $\cos x$ is 1, ($\alpha_q\beta_q$-$\alpha_p\beta_p$) and (z_q-z_p) are much smaller, Δx, Δy and Δz can be approximated as

$$\begin{cases} \Delta x = x_D - x_C \approx x_q - x_p + l\left(\alpha_q - \alpha_p\right) \\ \Delta y = y_D - y_C \approx y_q - y_p + l\left(\beta_q - \beta_p\right) \\ \Delta z = z_D - z_C \approx R_s\cos\theta\left(\beta_p - \beta_q\right) + R_s\sin\theta\left(\alpha_q - \alpha_p\right) \end{cases} \tag{A.4}$$

Then Δx^2, Δy^2 and Δz^2 are expressed as

$$\begin{cases} \Delta x^2 = \left(x_q - x_p\right)^2 + l^2\left(\alpha_q - \alpha_p\right)^2 + 2l\left(x_q - x_p\right)\left(\alpha_q - \alpha_p\right) \\ \Delta y^2 = \left(y_q - y_p\right)^2 + l^2\left(\beta_q - \beta_p\right)^2 + 2l\left(y_q - y_p\right)\left(\beta_q - \beta_p\right) \\ \Delta z^2 = R_s^2\cos^2\theta\left(\beta_q - \beta_p\right)^2 + R_s^2\sin^2\theta\left(\alpha_q - \alpha_p\right)^2 + 2R_s^2\sin\theta\cos\theta\left(\alpha_q - \alpha_p\right)\left(\beta_p - \beta_q\right) \end{cases} \tag{A.5}$$

Appendix B

The plane *OR* can be obtained by coordinate transformation as follows

$$\begin{cases} x_3' = x_3\cos\Delta\beta_{pq} + y_3\sin\Delta\alpha_{pq}\sin\Delta\beta_{pq} - z_3\cos\Delta\alpha_{pq}\sin\Delta\beta_{pq} \\ y_3' = y_3\cos\alpha_{pq} + z_3\sin\alpha_{pq} \\ z_3' = x_3\sin\beta - y_3\sin\alpha_{pq}\cos\Delta\beta_{pq} + z_3\cos\alpha_{pq}\cos\Delta\beta_{pq} \end{cases} \tag{B.1}$$

The parametric equation of the rotor's outer surface can be expressed as

$$\begin{cases} x_3 = R_s\cos\theta_3 \\ y_3 = -R_s\cos\theta_3 \end{cases} \quad \begin{cases} x_3' = R_s\cos\theta_3' \\ y_3' = -R_s\cos\theta_3' \end{cases} \tag{B.2}$$

Submitting Eq. (B.2) to Eq. (B.1), we can get

$$\begin{cases} R_s\cos\theta_3' = x_3\cos\Delta\beta_{pq} + y_3\sin\Delta\alpha_{pq}\sin\Delta\beta_{pq} - z_3\cos\Delta\alpha_{pq}\sin\Delta\beta_{pq} \\ -R_s\cos\theta_3' = y_3\cos\alpha_{pq} + z_3\sin\alpha_{pq} \end{cases} \tag{B.3}$$

Since $[R_s\cos(\theta_3)]^2$ + $[-R_s\sin(\theta_3)]^2 = 1$, the implicit function relationship between the z_3 and θ_3 can be expressed as

$$
\begin{aligned}
&R_s^2\cos^2\theta_3\cos^2\beta_{pq} + 2R_s^2\cos\theta_3\sin\theta_3\cos\beta_{pq}\sin\alpha_{pq}\sin\beta_{pq} + R_s^2\sin^2\theta_3\cos^2\alpha_{pq} + \\
&R_s^2\sin^2\theta_3\sin^2\alpha_{pq}\sin^2\beta_{pq} - R_s^2 + 2R_s\sin\theta_3\cdot z_3(\theta_3)\sin\alpha_{pq}\cos\alpha_{pq}\cos^2\beta_{pq} - \\
&2R_s\cos\theta_3\cdot z_3(\theta_3)\cos\alpha_{pq}\cos\beta_{pq}\sin\beta_{pq} + z_3^2(\theta_3)\sin^2\alpha_{pq} + z_3^2(\theta_3)\cos^2\alpha_{pq}\sin^2\beta_{pq} = 0
\end{aligned}
\tag{B.4}
$$

The implicit function is simplified to explicit function as

$$
z_3(\theta_3) = \frac{\pm\left[\left(\begin{array}{c} R_s^2 - 2R_s^2\cos\theta_3\sin\theta_3\cos\beta_{pq}\sin\alpha_{pq}\sin\beta_{pq} - \\ R_s^2\sin^2\theta_3\sin^2\alpha_{pq}\sin^2\beta_{pq} - 2R_s^2\sin\theta_3\cos\theta_3\sin\beta_{pq} \\ +R_s^2\cos^2\theta_3\sin^2\beta_{pq} - R_s^2\cos^2\theta_3\cos^2\beta_{pq} \end{array}\right)^{0.5} + R_s\cos\theta_3\sin\beta_{pq} - R_s\sin\theta_3\right]}{\cos\alpha_{pq}\sin\beta_{pq}}
\tag{B.5}
$$

Appendix C

The equations describing planes PA and PB in the absolute coordinate can be expressed as.

$$
\begin{cases} A_{33}x_3 + B_{33}y_3 + C_{33}z_3 + 1 = 0 \\ A_{44}x_3 + B_{44}y_3 + C_{44}z_3 + 1 = 0 \end{cases}
\tag{C.1}
$$

where A_{33}, B_{33}, C_{33}. A_{44}, B_{44}, C_{44} are all unknown coefficients. These coefficients can be obtained by taking the coordinates of three arbitrary points on one plane. Taking the plane PB for example, the three points $P_{B1}(x_{B1}, y_{B1}, z_{B1})$, $P_{B2}(x_{B2}, y_{B2}, z_{B2})$, $P_{B3}(x_{B3}, y_{B3}, z_{B3})$ are as follows,

$$
\begin{cases}
x_{B1} = L_{sr}\sin\Delta\alpha_{pq}\cos\Delta\beta_{pq}, y_{B1} = L_{sr}\sin\Delta\beta_{pq}, z_{B1} = L_{sr}\cos\Delta\alpha_{pq}\cos\Delta\beta_{pq} \\
x_{B2} = L_{sr}\sin\Delta\alpha_{pq}\cos\Delta\beta_{pq} + R_s\cos\Delta\beta_{pq}, y_{B2} = L_{sr}\sin\Delta\beta_{pq} + R_s\sin\Delta\alpha_{pq}\sin\Delta\beta_{pq}, \\
\qquad z_{B2} = L_{sr}\cos\Delta\alpha_{pq}\cos\Delta\beta_{pq} - R_s\sin\Delta\beta_{pq}\cos\Delta\alpha_{pq} \\
x_{B3} = L_{sr}\sin\Delta\alpha_{pq}\cos\Delta\beta_{pq}, y_{B3} = L_{sr}\sin\Delta\beta_{pq} + R_s\cos\Delta\alpha_{pq}, z_{B3} = L_{sr}\cos\Delta\alpha_{pq}\cos\Delta\beta_{pq} + R_s\sin\Delta\alpha_{pq}
\end{cases}
\tag{C.2}
$$

Since the nodes on the inner surface of the disk can be expressed as: $x_3^2 + y_3^2 = {R_s}^2$. The coordinate (x, y) on the line ls_2 can be transformed to $(R_s\cos\theta_3, R_s\sin\theta_3)$. The intersecting lines can be expressed as

$$
\begin{cases} W_1(\theta_3) = -(A_{33}R_s\cos\theta + B_{33}R_s\cos\theta_3 + 1)/C_{33} \quad (\theta_{31} \le \theta_3 < \theta_{32}) \\ W_2(\theta_3) = -(A_{44}R_s\cos\theta + B_{33}R_s\cos\theta_3 + 1)/C_{44} \quad (\theta_{32} \le \theta_3 < \theta_{31} + 2\pi) \end{cases}
\tag{C.3}
$$

Appendix D

The fractal parameters of disks with different contact radius are:

Thickness (mm)	Inner diameter (mm)	Fractal dimension D	Fractal roughness G (m)
2	16.000	1.457	1.02×10^{-10}
2	15.997	1.451	0.95×10^{-10}
2	15.995	1.454	1.05×10^{-10}
2	15.993	1.451	0.93×10^{-10}
2	15.990	1.457	0.86×10^{-10}
3	16.000	1.455	0.92×10^{-10}
3	15.997	1.454	0.96×10^{-10}
3	15.995	1.458	0.89×10^{-10}
3	15.993	1.455	1.09×10^{-10}
3	15.990	1.451	1.06×10^{-10}
4	16.000	1.453	0.86×10^{-10}
4	15.997	1.455	0.99×10^{-10}
4	15.995	1.454	1.01×10^{-10}
4	15.993	1.451	1.03×10^{-10}
4	15.990	1.454	0.98×10^{-10}

The detailed values of the main parameters in the simulation and experiments:

Main parameter	Value
Displacement stiffness of AMB $-\ k_h$	1.81×10^6N•m^{-1}
Current stiffness of AMB $-\ k_i$	287.76 N•A^{-1}
Gain of the displacement sensor $-\ k_s$	20000 V•m^{-1}
Gain of the power amplifier $-\ k_a$	0.36
Cut-off frequency of the power amplifier $-\ f_z$	800 Hz
Proportional gain of the PID controller $-\ K_P$	1.7
Integral gain of the PID controller $-\ K_I$	1
Derivative gain of the PID controller $-\ K_D$	0.0006
Derivative time constant of the PID controller $-\ T_D$	0.0001

Appendix E

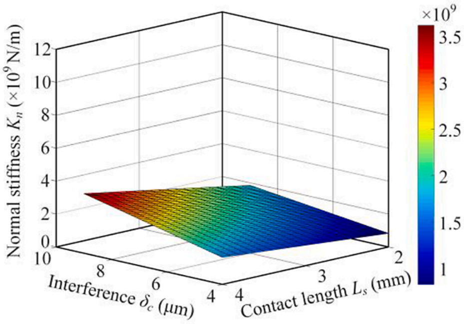

(a) Normal stiffness under different interferences and contact lengths

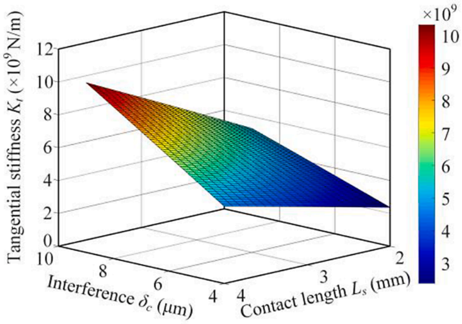

(b) Tangential stiffness under different interferences and contact lengths

References

[1] G. Schweitzer, E.H. Maslen, Magnetic Bearings: Theory, Design, and Application to Rotating Machinery, Springer, Berlin, 2009.
[2] J. Li, S. Wang, Z. Li, Y. Yu, X. Cheng, Analysis of axial holding capability about the lengthened shrink-fit holder and cutting tool system, Adv. Mater. Res. (switzerland) 940 (2014) 249–253, https://doi.org/10.4028/www.scientific.net/AMR.940.249.
[3] J.S. Paul, Applying API 617, 8th Edition to Expander-Compressors with Active Magnetic Bearings, 44th Turbomachinery Symposium: TPS 2015, Houston, Texas, USA, 2015, pp. 349-364.
[4] S. Wei, J. Zhou, X. Han, S. Zheng, A simplified analysis method and suppression of the modalities of a magnetic levitation turbo rotor system, Vacuum 217 (2023), https://doi.org/10.1016/j.vacuum.2023.112452.
[5] L. Gaul, A. Schmidt, Finite element simulation and experiments on rotor damping assembled by disc shrink fits, Mech. Syst. Sig. Process. 127 (2019) 412–422, https://doi.org/10.1016/j.ymssp.2018.11.021.
[6] Y. Xu, J. Zhou, L. Di, C. Zhao, Q. Guo, Active Magnetic Bearing Rotor Model Updating Using Resonance and MAC Error, Shock Vib. 2015 (2015) 1–9, https://doi.org/10.1155/2015/263062.
[7] Y. Zhang, J. Zhou, Y. Zhang, Y. Zhou, Y. Xu, Modelling and vibration response of a magnetically suspended flexible rotor considering base motion, App. Math. Model. 118 (2023) 518–540, https://doi.org/10.1016/j.apm.2023.01.020.
[8] T. Li, Z. Xu, J. Guan, J. Song, Current Research State on Interface Dynamics of Spindle-Toolholder, Advanced Manufacturing and Automation XI, Lecture Notes in Electrical Engineering (880) (2022) 472–478, https://doi.org/10.1007/978-981-19-0572-8_60.
[9] S.M.M. Jafri, J.M. Vance, Asme, Shrink Fit Effects on Rotordynamic Stability: Theoretical Study, 53rd ASME Turbo Expo 2008, Berlin, Germany, 2008, pp. 1017-1024. https://doi.org/10.1115/GT2008-50412.
[10] F. Sorge, Stability analysis of rotor whirl under nonlinear internal friction by a general averaging approach, J. Vib. Control 23 (2016) 808–826, https://doi.org/10.1177/1077546315583752.
[11] F. Sorge, Nonlinear analysis of cylindrical and conical hysteretic whirl motions in rotor-dynamics, J. Sound Vib. 333 (2014) 5042–5056, https://doi.org/10.1016/j.jsv.2014.05.016.
[12] M. Namazi, Y. Altintas, T. Abe, N. Rajapakse, Modeling and identification of tool holder–spindle interface dynamics, Int J Mach Tool Manu 47 (2007) 1333–1341, https://doi.org/10.1016/j.ijmachtools.2006.08.003.
[13] O. Özşahin, Y. Altintas, Prediction of frequency response function (FRF) of asymmetric tools from the analytical coupling of spindle and beam models of holder and tool, Int J Mach Tool Manu 92 (2015) 31–40, https://doi.org/10.1016/j.ijmachtools.2015.03.001.
[14] E. Sikanen, J.E. Heikkinen, J. Sopanen, Shrink-fitted joint behavior using three-dimensional solid finite elements in rotor dynamics with inclusion of stress-stiffening effect, Adv. Mech. Eng. 10 (2018), https://doi.org/10.1177/1687814018780054.
[15] E. Sikanen, J.E. Heikkinen, J. Sopanen, Effect of Operational Temperature on Contact Dynamics of Shrink-Fitted Compressor Impeller Joint, Advances in Mechanism and Machine Science (2019) 3341–3351, https://doi.org/10.1007/978-3-030-20131-9_330.
[16] P. Yu, L. Li, G. Chen, M. Yang, Dynamic modelling and vibration characteristics analysis for the bolted joint with spigot in the rotor system, App. Math. Model. 94 (2021) 306–331, https://doi.org/10.1016/j.apm.2021.01.028.
[17] Z. Han, D. Wang, Y. Wang, J. Hong, R. Cheng, Dynamic effects of the initial skewness of the inertial principal axis on the rotor with bolted joint, Mech. Syst. Sig. Process. 200 (2023), https://doi.org/10.1016/j.ymssp.2023.110564.
[18] X. Gao, M. Wang, Y. Zhang, T. Zan, A modeling approach for contact stiffness of spindle–tool holder based on fractal theory, Proc. Inst. Mech. Eng., Part B: J. Eng. Manuf., 230 (2016) 1942-1951. https://doi.org/10.1177/0954405415579009.

[19] G. Zhao, Z. Xiong, X. Jin, L. Hou, W. Gao, Prediction of contact stiffness in bolted interface with natural frequency experiment and FE analysis, Tribol. Int. 127 (2018) 157–164, https://doi.org/10.1016/j.triboint.2018.05.044.
[20] K. Jiang, Z.F. Liu, Y. Tian, T. Zhang, C.B. Yang, An estimation method of fractal parameters on rough surfaces based on the exact spectral moment using artificial neural network, Chaos Solitons Fractals 161 (2022), https://doi.org/10.1016/j.chaos.2022.112366.
[21] J. Liao, J. Zhang, P. Feng, D. Yu, Z. Wu, Identification of contact stiffness of shrink-fit tool-holder joint based on fractal theory, Int. J. Adv. Manuf. Technol. 90 (2016) 2173–2184, https://doi.org/10.1007/s00170-016-9506-3.
[22] Y. Zhao, J. Xu, L. Cai, W. Shi, Z. Liu, Q. Cheng, Contact characteristic analysis of spindle–toolholder joint at high speeds based on the fractal model, Proceedings of the Institution of Mechanical Engineers, Part e: Journal of Process Mechanical Engineering 231 (2016) 1025–1036, https://doi.org/10.1177/0954408916652648.
[23] J. Liu, C. Ma, S. Wang, S. Wang, B. Yang, Contact stiffness of spindle-tool holder based on fractal theory and multi-scale contact mechanics model, Mech. Syst. Sig. Process. 119 (2019) 363–379, https://doi.org/10.1016/j.ymssp.2018.09.037.
[24] Y. Liu, H. Liu, J. Yi, M. Jing, Investigation on the stability and bifurcation of a rod-fastening rotor bearing system, J. Vib. Control 21 (2014) 2866–2880, https://doi.org/10.1177/1077546313518817.
[25] L. Li, Z. Luo, F. Wu, F. He, K. Sun, Frequency spectrum analysis of the rotor system with bolted joint: Numerical and experimental verification, App. Math. Model. 118 (2023) 745–761, https://doi.org/10.1016/j.apm.2023.02.003.
[26] X. Wu, Y. Jiao, Z. Chen, W. Ma, Establishment of a contact stiffness matrix and its effect on the dynamic behavior of rod-fastening rotor bearing system, Arch. Appl. Mech. 91 (2021) 3247–3271, https://doi.org/10.1007/s00419-021-01963-9.
[27] W. Shi, Z. Zhang, An improved contact parameter model with elastoplastic behavior for bolted joint interfaces, Compos. Struct. 300 (2022), https://doi.org/10.1016/j.compstruct.2022.116178.
[28] S. Jiang, Y. Zheng, H. Zhu, A contact stiffness model of machined plane joint based on fractal theory, J. Tribol. 132 (2009), https://doi.org/10.1115/1.4000305.
[29] M. Lalanne and G. Ferraris, Rotordynamics Prediction in Engineering. 2nd Edition, John Wiley & Sons, 252p (1998).
[30] D. Li, D. Botto, R. Li, C. Xu, W. Zhang, Experimental and theoretical studies on friction contact of bolted joint interfaces, Int. J. Mech. Sci. 236 (2022), https://doi.org/10.1016/j.ijmecsci.2022.107773.
[31] Mechanical vibration—Vibration of rotating machinery equipped with active magnetic bearings-Part 3: Evaluation of stability margin: ISO 14839-3. London: British Standard Institution, 2006.